JCI The Journal of Clinical Investigation

Striatal Kir2 K^+ channel inhibition mediates the antidyskinetic effects of amantadine

Weixing Shen, … , Alfred L. George Jr., D. James Surmeier

J Clin Invest. 2020;130(5):2593-2601. https://doi.org/10.1172/JCI133398.

Research Article **Neuroscience**

Levodopa-induced dyskinesia (LID) poses a significant health care challenge for Parkinson's disease (PD) patients. Amantadine is currently the only drug proven to alleviate LID. Although its efficacy in treating LID is widely assumed to be mediated by blockade of *N*-methyl-D-aspartate (NMDA) glutamate receptors, our experiments demonstrate that at therapeutically relevant concentrations, amantadine preferentially blocks inward-rectifying K^+ channel type 2 (Kir2) channels in striatal spiny projection neurons (SPNs) — not NMDA receptors. In so doing, amantadine enhances dendritic integration of excitatory synaptic potentials in SPNs and enhances — not antagonizes — the induction of long-term potentiation (LTP) at excitatory, axospinous synapses. Taken together, our studies suggest that the alleviation of LID in PD patients is mediated by diminishing the disparity in the excitability of direct- and indirect-pathway SPNs in the on state, rather than by disrupting LTP induction. This insight points to a pharmacological approach that could be used to effectively ameliorate LID and improve the quality of life for PD patients.

Striatal Kir2 K+ channel inhibition mediates the antidyskinetic effects of amantadine

Weixing Shen,[1] Wenjie Ren,[1] Shenyu Zhai,[1] Ben Yang,[1] Carlos G. Vanoye,[2] Ananya Mitra,[3] Alfred L. George Jr.,[2] and D. James Surmeier[1]

[1]Department of Physiology and [2]Department of Pharmacology, Feinberg School of Medicine, Northwestern University, Chicago, Illinois, USA. [3]Adamas Pharmaceuticals, Inc., Emeryville, California, USA.

Levodopa-induced dyskinesia (LID) poses a significant health care challenge for Parkinson's disease (PD) patients. Amantadine is currently the only drug proven to alleviate LID. Although its efficacy in treating LID is widely assumed to be mediated by blockade of *N*-methyl-D-aspartate (NMDA) glutamate receptors, our experiments demonstrate that at therapeutically relevant concentrations, amantadine preferentially blocks inward-rectifying K+ channel type 2 (Kir2) channels in striatal spiny projection neurons (SPNs) — not NMDA receptors. In so doing, amantadine enhances dendritic integration of excitatory synaptic potentials in SPNs and enhances — not antagonizes — the induction of long-term potentiation (LTP) at excitatory, axospinous synapses. Taken together, our studies suggest that the alleviation of LID in PD patients is mediated by diminishing the disparity in the excitability of direct- and indirect-pathway SPNs in the on state, rather than by disrupting LTP induction. This insight points to a pharmacological approach that could be used to effectively ameliorate LID and improve the quality of life for PD patients.

Introduction

Parkinson's disease (PD) is the second most common neurodegenerative disease (1, 2). The cardinal motor symptoms of PD are caused by the degeneration of dopaminergic neurons in the substantia nigra. In the initial stages of the disease, levodopa treatment effectively ameliorates PD motor symptoms by restoring tonic brain dopamine (DA) levels. But as the disease progresses, the dose of levodopa required to achieve symptomatic benefit increases. With oral administration of high doses of levodopa, many patients experience paradoxical, involuntary movements or dyskinesia (3). At present, the only proven pharmacological strategy for reducing this levodopa-induced dyskinesia (LID) is coadministration of amantadine (AMT) (4).

AMT is widely thought to exert its antidyskinetic effects by blunting aberrant synaptic plasticity induced in the striatum by levodopa treatment (5, 6). The logic behind this view is simple. In PD models, prolonged elevation of striatal DA (subsequent to levodopa treatment) promotes the induction of long-term potentiation (LTP) of glutamatergic synapses on direct-pathway spiny projection neurons (dSPNs) (7–9). Unlike the situation in the normal brain where DA sculpts striatal action selection circuitry in response to experience, the levodopa-induced elevation is disconnected from experience, disrupting normal patterns of connectivity. As dSPNs anchor the basal ganglia circuitry that promotes movement, the aberrant strengthening of their excitatory synapses is thought to promote inappropriate movement or dyskinesia. Therefore, one way to diminish LID is to blunt the induction of LTP following levodopa treatment. In dSPNs, LTP induction depends on stimulation of both D1 DA receptors (D1Rs) and *N*-methyl-D-aspartate receptors (NMDARs) (10–12). As AMT is a low-affinity, noncompetitive antagonist of NMDARs (13, 14), it is hypothesized to suppress LID by blocking NMDARs and the induction of disruptive synaptic plasticity following levodopa treatment.

As appealing as this model is, there are reasons for doubt. First, the network pathophysiology underlying LID involves not just dSPN ensembles, but other striatal cell types as well, including indirect-pathway spiny projection neurons (iSPNs) (8, 15, 16). For example, enhancing the excitability of iSPNs alleviates LID in mouse models (15). Second, AMT is known to interact with other membrane proteins including voltage-dependent K+ channels that could shape neuronal excitability, raising questions about its specificity of action (17–19). Moreover, within the clinically relevant concentration range (<50 μM) (20, 21), it is unclear whether AMT effectively blocks synaptic NMDARs controlling plasticity.

The experiments described here were designed to test the hypothesis that at therapeutically relevant concentrations, AMT effectively blocks synaptic NMDARs and disrupts the ability to induce LTP at glutamatergic synapses on dSPNs. Using a combination of pharmacological, optical, and electrophysiological approaches, our experiments strongly suggest that this hypothesis is false. Rather, our studies revealed that at pharmaceutically relevant drug concentrations, AMT blocked Kir2 channels that control the intrinsic excitability of SPNs, without significantly diminishing synaptic NMDAR currents. Moreover, through this mechanism, AMT enhanced the induction of LTP in iSPNs, without diminishing LTP induction in dSPNs in tissue from both naive and dyskinetic mice. Our results support the proposition that the

Conflict of interest: The authors have declared that no conflict of interest exists.

Submitted: September 10, 2019; **Accepted:** February 6, 2020; **Published:** April 20, 2020.
Reference information: *J Clin Invest*. 2020;130(5):2593–2601.
https://doi.org/10.1172/JCI133398.

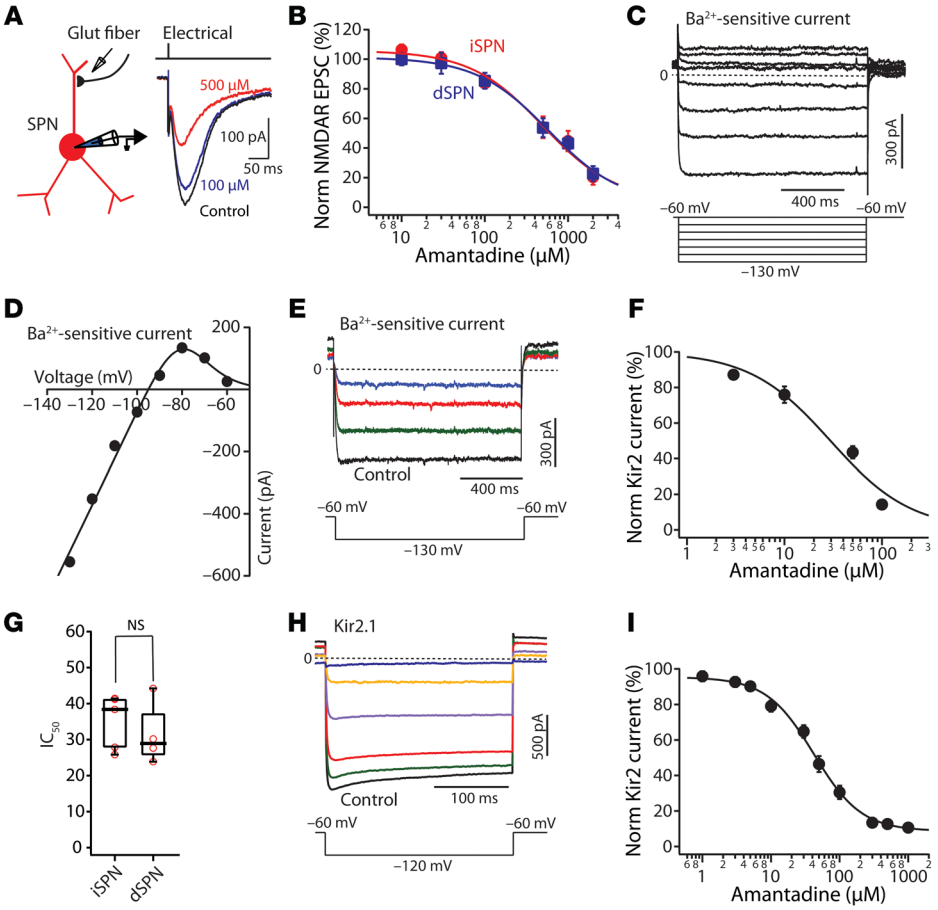

Figure 1. AMT preferentially blocks inwardly rectifying Kir2 channels at therapeutically relevant concentrations. (**A**) The experimental configuration. Representative traces showing the control NMDAR-mediated synaptic current and the currents evoked after application of the labeled doses of AMT. (**B**) Dose-response relationship of the AMT modulation of NMDAR-mediated current in dSPNs and iSPNs. IC_{50} = 641 μM (iSPN n = 5–10); IC_{50} = 648 μM (dSPN n = 5–11). (**C**) Current-voltage relationship at negative membrane potentials revealed an inwardly rectifying current. Cells were held at –60 mV and stepped up to –130 mV in –10-mV increments in the presence of tetrodotoxin (1 μM). Subsequent bath application of Ba^{2+} (200 μM) blocked all Kir2 channel currents, leaving currents attributable to KCNK channels. Subtraction of the records before and after Ba^{2+} application showed a Ba^{2+}-sensitive Kir2 current. (**D**) The Ba^{2+}-subtracted current plotted against the step potential. The data points were fit with a Boltzmann equation. (**E**) The Kir2 current evoked by a voltage steps from –60 mV to –130 mV was reduced by a range of AMT concentrations (10, 50, or 100 μM). (**F**) Dose-response relationship of the AMT suppression of Kir2 current. IC_{50} = 29 μM (n = 4–6). (**G**) Box plot showing the effect of AMT on IC_{50}s between iSPNs and dSPNs (iSPN n = 5, dSPN n = 4, $P > 0.05$ by Mann-Whitney test). NS, not significant. (**H**) Average Ba^{2+}-sensitive currents recorded at –120 mV from CHO-K1 cells stably expressing Kir2.1 and exposed to vehicle, 3, 10, 100, 500, or 3000 μM AMT. (**I**) Dose-response curve of Kir2.1 current measured after exposure to various AMT concentrations (n = 12–23) and IC_{50} = 38.3 ± 3.1 μM. Data are shown as mean ± SEM.

disparity in the excitability of iSPNs and dSPNs in the on state contributes to the emergence of dyskinetic behavior and clearly point to alternative strategies for alleviating LID in humans.

Results

AMT preferentially blocks Kir2 K^+ channels. To assess the ability of AMT to antagonize NMDAR-mediated excitatory postsynaptic currents (EPSCs), striatal SPNs were interrogated in ex vivo corticostriatal parasagittal brain slices from *Drd1a* or *Drd2* bacterial artificial chromosome–transgenic (BAC-transgenic) mice; in these mice, dSPNs and iSPNs are labeled with tdTomato and enhanced green fluorescent protein (EGFP), respectively (22, 23). NMDAR-mediated EPSCs were evoked by intrastriatal stimulation of glutamatergic afferent fibers in the presence of 0.2–1 mM Mg^{2+}, the AMPA receptor (AMPAR) antagonist NBQX (10 μM), and the $GABA_A$ receptor blocker gabazine (10 μM) (Figure 1A). At a holding membrane potential of –40 mV, NMDAR synaptic currents had a moderate sensitivity to AMT in both dSPNs and iSPNs (Figure 1, A and B). The dose-response relationship could be well fit by a logistic equation of the following form: $Y = ([Y_0 - Y_\infty]/ [1 + (C \times IC_{50}^{-1})^B]) + Y_\infty$, where Y_0 is the amplitude in the absence of AMT, Y_∞ is the maximal response to AMT, B is the slope factor, and C is the concentration of AMT. The IC_{50} values were 648 μM in iSPNs (n = 5–10) and 641 μM in dSPNs (n = 5–11) (Figure 1B).

Surprisingly, these IC_{50} values are much higher than those reported in the studies characterizing the pharmacological action of AMT (13, 14, 24). However, the previous studies were performed in the absence of extracellular Mg^{2+} and engaged extrasynaptic NMDARs. Both Mg^{2+} and AMT bind deep within the channel pore at a region near the selectivity filter of the NMDAR channel and may competitively interact. As a consequence, therapeutically relevant AMT concentrations might have few effects on NMDAR-mediated synaptic responses in vivo. Indeed, the IC_{50} of AMT for NMDARs in our experiments was roughly an order of magnitude higher than the AMT concentration needed to achieve therapeutic benefit (20, 21).

If AMT is not targeting NMDARs, then what is it targeting? AMT was originally introduced as an antiviral medication whose action was thought to be mediated by blockade of a miniature K^+ channel, Kcv (17). This viral K^+ channel is homologous to the inwardly rectifying Kir2 K^+ channel found in SPNs (17, 25). To test the possible interaction of AMT with Kir2 K^+ channels, SPNs were held in voltage clamp at a relatively depolarized potential (–60 mV) to inactivate Kv1 and Kv4 K^+ channels and then stepped to a hyperpolarized potential. The Mg^{2+} and polyamine block of Kir2 K^+ channels at depolarized membrane potentials is rapidly relieved by hyperpolarization, leading to a sustained inward current (ref. 26 and Figure 1C). Bath application of Ba^{2+} (200 μM) blocked the Kir2 channel current, leaving

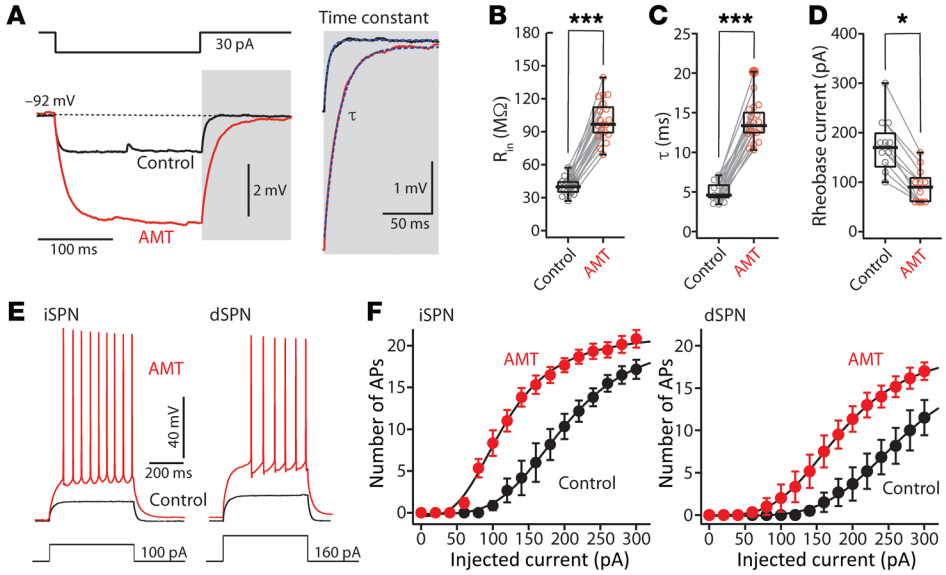

Figure 2. AMT increased somatic excitability in dSPNs and iSPNs. (**A**) Current-clamp analysis of membrane input resistance (R_{in}) and time constant (τ) at SPN resting membrane potential. AMT (100 μM) increased both R_{in} (**B**) (control n = 19, AMT = 19) and τ (**C**) (control n = 19, AMT = 19). (**D**–**F**) Somatic excitability of SPNs was increased by AMT (100 μM) in both iSPNs and dSPNs. Somatic excitability was assessed by somatic current injection before and after application of 100 μM AMT. (**D**) AMT reduced rheobase current (control n = 12, AMT = 12). (**E**) Sample voltage recordings in response to a 100-pA current injection in an iSPN and a 160-pA current injection in a dSPN. (**F**) Effect of 100 μM AMT on the number of action potentials (APs) evoked by 500-ms current injections (iSPN n = 6, dSPN n = 6). *P < 0.05, ***P < 0.001 by Mann-Whitney test.

currents attributable to KCNK channels (25, 27). Subtraction of the records before and after Ba^{2+} application revealed a strongly inwardly rectifying, K^+-selective current (Figure 1, C and D). A plot of current amplitude as a function of voltage could be readily fit with a Boltzmann equation (Figure 1D).

Bath application of AMT reduced the inwardly rectifying Kir2 K^+ current in SPNs in a dose-dependent manner (Figure 1, E–G). Subsequent application of Ba^{2+} blocked the remaining portion of the Kir2 K^+ channel current. Using the Ba^{2+}-sensitive currents, an AMT dose-response curve was constructed. The fitted IC_{50}s of AMT for the Kir2 K^+ channels were not different between iSPNs and dSPNs (Figure 1G). More importantly, the calculated IC_{50}s of AMT were roughly 20 times lower than that for NMDARs and close to that needed to achieve symptomatic benefit (20, 21).

To provide an independent assessment of the AMT dose-response relationship, Kir2.1 K^+ channels were heterologously expressed in Chinese hamster ovary (CHO-K1) cells; these cells were patch clamped to generate currents and AMT bath applied at a range of concentrations (Figure 1, H and I). This heterologous Kir2.1 channel dose-response curve for AMT yielded a very similar value to that obtained from natively expressed Kir2 K^+ channels in SPNs (Figure 1, E–G). Taken together, these data strongly support the proposition that AMT is a high-affinity blocker of Kir2 K^+ channels expressed in SPNs.

AMT increased somatic excitability in iSPNs and dSPNs. To appraise the effects of AMT on neuronal excitability, whole-cell current clamp recordings were made from SPNs in ex vivo brain slices (Figure 2). A small hyperpolarizing current step from the resting membrane potential was used to estimate the membrane input resistance and time constant (τ). Bath application of AMT significantly increased both input resistance and membrane time constant (R_{in}: control n = 19, AMT n = 19, P < 0.001 by Mann-Whitney rank-sum test; τ: control n = 19, AMT n = 19, P < 0.001 by Mann-Whitney test) (Figure 2, B and C). Moreover, AMT (100 μM) significantly decreased the rheobase current in both dSPNs and iSPNs (control n = 12, AMT n = 12, P < 0.05 by Mann-Whitney test) (Figure 2D).

To determine how the larger input resistance translated to spiking, current steps of escalating amplitude were injected through the somatic patch electrode and the resulting spiking measured. In control SPNs, the relationship between injected current and spike frequency was similar to that described in previous studies (28, 29). Bath application of AMT (100 μM) substantially increased intrinsic excitability, shifting the frequency-intensity relationship to the left in both iSPNs and dSPNs (Figure 2, E and F).

AMT block of Kir2 channels enhanced dendritic excitability. Kir2 K^+ channels are distributed throughout the somatodendritic membrane of SPNs. In dendrites, Kir2 channels hold the membrane potential near the K^+ equilibrium potential at rest and provide a constitutively active leak that dissipates currents coming from other parts of the cell and through local synaptic glutamate receptors (25). To directly assess the effects of AMT on these features of SPN dendrites, 4 approaches were used.

First, SPNs were loaded with a K^+-based internal solution containing the Ca^{2+}-insensitive red fluorophore Alexa Fluor 568 (50 μM) and imaged using 2-photon laser scanning microscopy (2PLSM). This allowed visualization of dendrites and spines. Next, 2PLSM was used in conjunction with the Ca^{2+}-sensitive green fluorophore Fluo-4 (100 μM) to monitor changes in cytosolic Ca^{2+} concentration ($[Ca^{2+}]$) in dendrites evoked by a somatically triggered, back-propagating action potential (bAP). In both types of SPN, AMT increased the invasion of bAPs into the distal dendrites, resulting in significant elevation in the bAP-evoked distal dendritic $[Ca^{2+}]$ transient (Figure 3, A–D).

Second, to directly assess the ability of AMT to increase dendritic input resistance, 4-methoxy-7-nitroindolinyl–caged L-glutamate (MNI-glutamate) was uncaged at the head of visualized spines using a 2-photon laser pulse (Figure 3E). As predicted, bath application of AMT (100 μM) significantly increased the amplitude of these uncaging evoked excitatory postsynaptic potentials (uEPSPs) (n = 12, P < 0.001 by Wilcoxon's test) (Figure 3, F and G).

Third, to test the hypothesis that AMT would increase the temporal summation of synaptically generated EPSPs, minimal local electrical stimulation of glutamatergic afferent fibers was performed

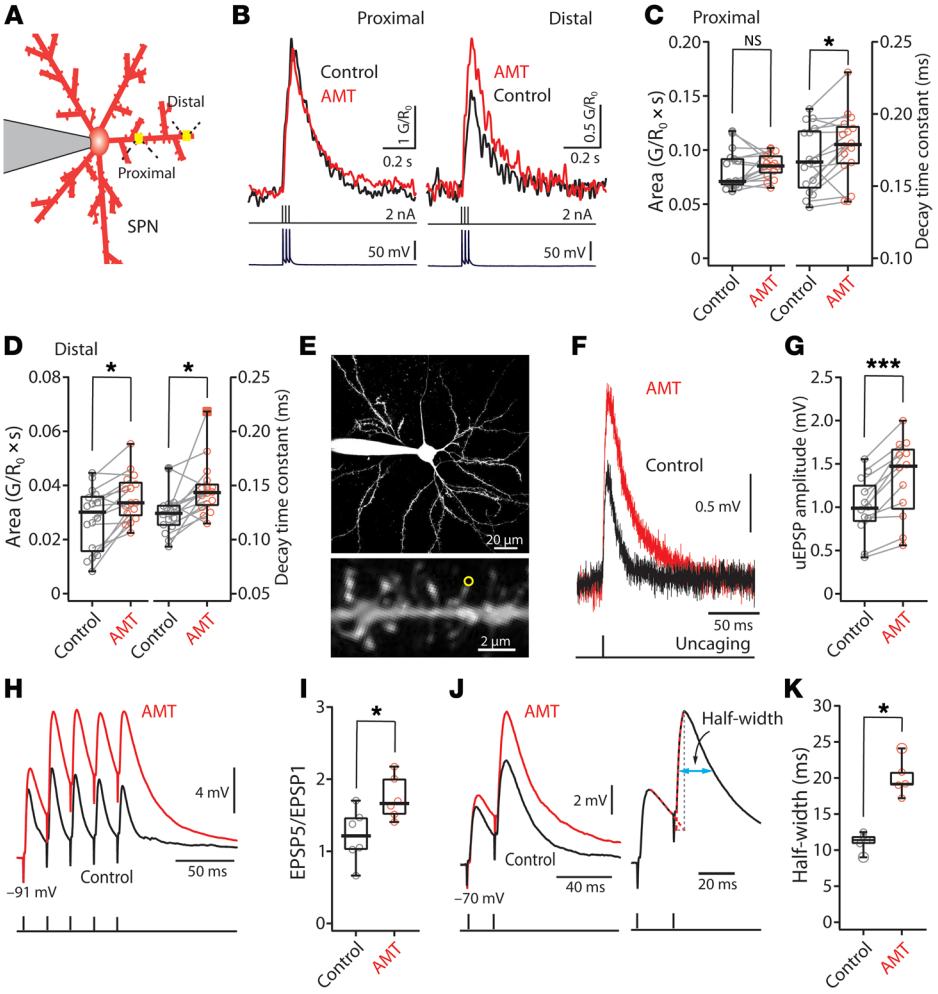

Figure 3. Blocking Kir2 current enhanced dendritic excitability in SPNs. (**A**) Schematic depicting the calcium imaging assay. (**B**) Sample bAP-evoked Ca^{2+} transients (top) before (black) and after application of 100 μM AMT (red). The current injection (middle) and voltage recordings (bottom) are also shown in temporal registration. (**C** and **D**) Box plots showing the effect of AMT on bAP-evoked Ca^{2+} transients in proximal (**C**) and distal (**D**) dendrites. AMT significantly increases Ca^{2+} transients only in distal dendrites, while it slows calcium transient decay in both proximal and distal dendrites (n = 16 dendrites from 8 cells). (**E**–**G**) AMT (100 μM) enhances distal uncaging-evoked synaptic response. (**E**) Low (top) and high (bottom) magnification maximum-intensity projections of an iSPN filled with Alexa Fluor 568. A single spine (indicated with a yellow circle) was stimulated with 1-ms uncaging laser pulses. (**F**) Sample somatic voltage recordings in response to glutamate uncaging. (**G**) Box plot showing the effect of AMT (100 μM) (n = 12 spines from 7 cells). NS, not significant. (**H**–**K**) EPSP trains were evoked by local stimulation of glutamatergic afferent fibers at 50 Hz. AMPAR-mediated input was isolated by application of antagonists. (**H** and **I**) At resting membrane potentials (approximately –90 mV), EPSPs summed sublinearly with the EPSP5/EPSP1 ratio between 1 and 2. AMT (100 μM) increased EPSP summation in iSPNs. The EPSP5/EPSP1 ratio increased in the presence of AMT (control n =6, AMT n = 6). (**J** and **K**) EPSPs before (black) and after (red) AMT application in which V_m was held constant at –70 mV. AMT (100 μM) significantly increased the half-width of the second EPSPs (control n = 5, AMT n = 5). *P < 0.05; ***P < 0.001 by Wilcoxon's test (**C**, **D**, and **G**) or Mann-Whitney test (**I** and **K**).

while monitoring somatic membrane potential. Glutamatergic EPSPs were isolated by bath application of antagonists for metabotropic glutamate receptors ($mGluR_1$ and $mGluR_5$), and $GABA_A$ and $GABA_B$ receptors. In control conditions, evoked EPSPs summed sublinearly, with the ratio of the fifth to the first EPSP (EPSP5/EPSP1) falling typically between 1 and 2 (Figure 3I). Bath application of AMT (100 μM) increased the amplitude of the first EPSP in the stimulus train and significantly increased the EPSP5/EPSP1 ratio (Figure 3I) (control n = 6, AMT n = 6, P < 0.05 by Mann-Whitney test).

Lastly, to assess the impact of AMT on summation of EPSPs at more depolarized membrane potentials, SPNs were held at –70 mV and a pair of stimuli delivered using minimal local stimulation. Bath application of AMT (100 μM) significantly increased the amplitude of the evoked EPSPs and prolonged the EPSP half-width (Figure 3, J and K) (control n = 5, AMT n = 5, P < 0.05 by Mann-Whitney test).

AMT promoted LTP induction. The results presented thus far indicate that at therapeutically relevant concentrations AMT effectively blocks Kir2 K^+ channels, but not NMDARs. As Kir2 channels determine the resting membrane potential and dendritic input resistance of SPNs, blocking them effectively increased input resistance and slowed the decay of membrane potential. These changes enhanced the summation of EPSPs (Figure 3). This enhanced summation should enhance NMDAR currents by dislodging Mg^{2+} blockade (30, 31). The slowing of the membrane time constant by AMT also could disrupt the Hebbian features of spike timing–dependent synaptic plasticity (STDP) in SPNs (11, 30). That is, by prolonging the membrane depolarization produced by a bAP, the release of glutamate after the bAP might still generate significant current through NMDARs, in contrast to the normal situation where the membrane potential had decayed to values in which Mg^{2+} blockade of NMDARs was prominent (30). In this situation, rather than inducing long-term depression (LTD), STDP pairing protocols in which bAPs preceded a glutamatergic EPSP could induce LTP.

To test this hypothesis, SPNs were studied using perforated-patch techniques in ex vivo brain slices (8, 11). As previously described, repeated (5 Hz) pairing of a bAP burst (generated by intrasomatic current injection) with a trailing (10 ms) EPSP (evoked by a glass electrode positioned near a proximal dendrite) induced a robust LTD (Figure 4, A and B). However, in the presence of AMT (100 μM), this same protocol induced LTP (Figure 4, C and D). To determine whether a similar phenomenon could be present in the dyskinetic state, these experiments were repeated in ex vivo brain slices obtained from a mouse model of LID 1 hour after the last injection of levodopa (8). As in slices from naive mice, the pairing of

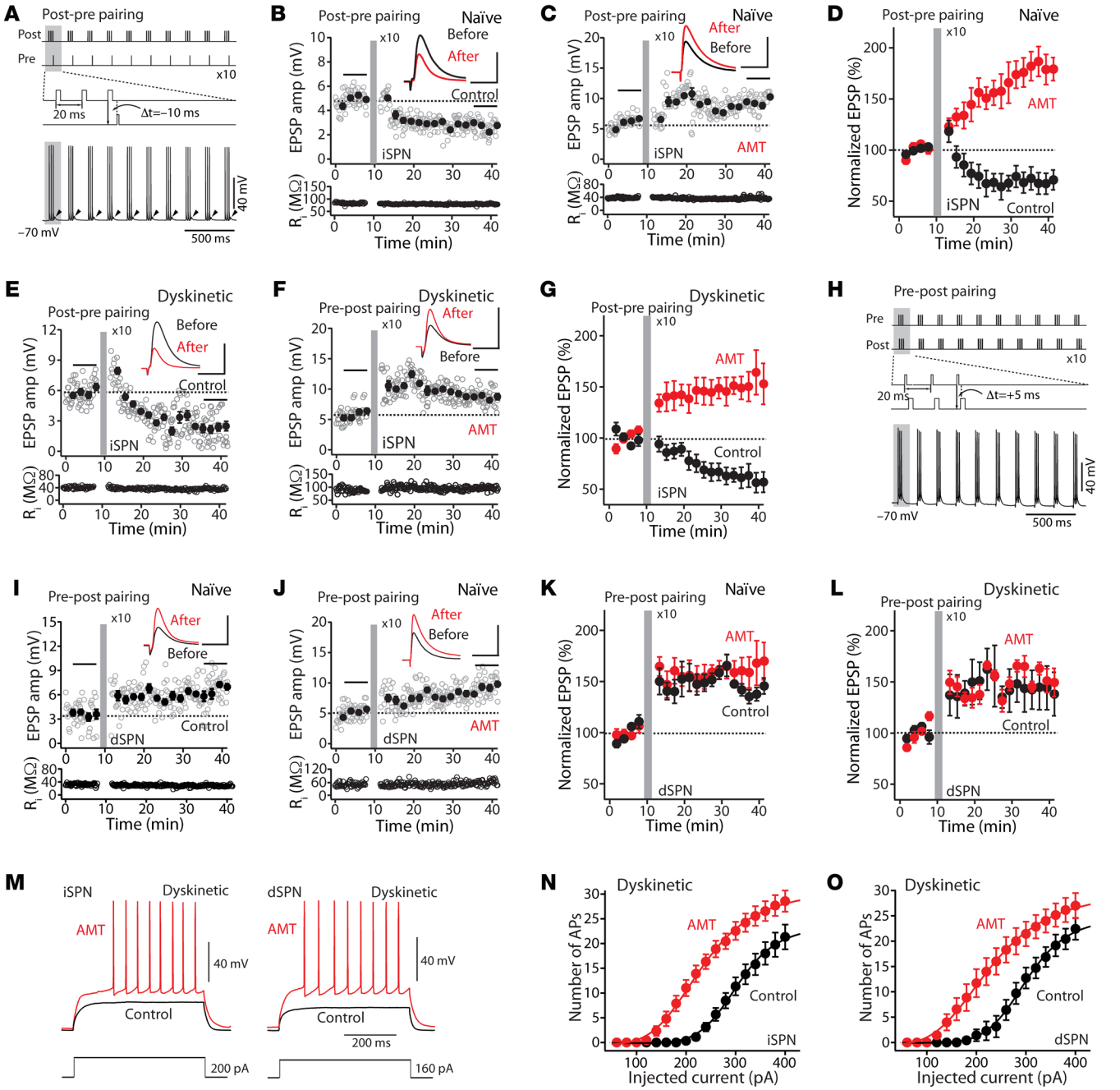

Figure 4. AMT promoted LTP induction. (**A**) Schematic illustrating the LTD induction protocol. (**B**) LTD was induced by a pre-post timing pairing in iSPNs. Plots show EPSP amplitude (amp) and input resistance (R_i) as a function of time. Scale bars: 3 mV × 50 ms. (**C**) In the presence of AMT (100 μM), the post-pre timing pairing revealed LTP. Scale bars: 4 mV × 60 ms. (**D**) In control, post-pre pairing revealed LTD in iSPNs, whereas in AMT, the same protocol promoted LTP (control $n = 4$, AMT $n = 5$, $P < 0.05$ by Mann-Whitney test). Data are represented as mean ± SEM. (**E**) The post-pre pairing induced LTD. Scale bars: 4 mV × 50 ms. (**F**) In contrast, AMT (100 μM) promoted induction of iSPN LTP in the dyskinetic state. Scale bars: 5 mV × 60 ms. (**G**) Plot of the average EPSP amplitudes as a function of time. Data are shown as mean ± SEM. Control $n = 6$, AMT $n = 7$, $P < 0.05$ by Mann-Whitney test. (**H**) Schematic depicting the LTP induction protocol. (**I**) LTP was induced by a pre-post pairing in dSPNs. Scale bars: 5 mV × 60 ms. (**J**) In the presence of AMT (100 μM), the pre-post pairing led to LTP. Scale bars: 4 mV × 60 ms. In both naive (**K**) and dyskinetic (**L**) animals, pre-post pairing induced dSPN LTP. Bath application of AMT (100 μM) did not alter LTP induction in either naive or LID tissue (naive: control $n = 5$, AMT $n = 6$, $P > 0.05$ by Mann-Whitney test. Dyskinetic: control $n = 5$, AMT $n = 6$, $P > 0.05$ by Mann-Whitney test). (**M**) Sample voltage recordings. (**N** and **O**) Effect of 100 μM AMT on the number of APs (iSPN $n = 9$, dSPN $n = 6$) in the dyskinetic state.

bAP bursts with a following EPSP induced a robust LTD in iSPNs (Figure 4, E and G). However, in the presence of AMT (100 μM), the same protocol induced a robust LTP in iSPNs, as in naive mice (Figure 4, F and G).

To verify that AMT was not having an unexpected effect on NMDARs in dSPNs, these cells were studied using the same approaches. In ex vivo brain slices from both naive and LID mice, pairing a presynaptic spike with a trailing postsynaptic spike

induced a potent LTP (Figure 4, H, I, K, and L), as shown previously (8). Bath application of AMT (100 μM) did not significantly alter LTP induction in either naive or LID tissue (Figure 4, H and J–L).

Finally, to determine how the modification in corticostriatal glutamatergic synaptic plasticity translated into spiking activity, the relationship between injected current and spike frequency was assessed in ex vivo brain slices from dyskinetic mice. As in naive tissue (Figure 2, E and F), AMT (100 μM) shifted the relationship to the left in both types of SPN (Figure 4, M–O).

Discussion

Contrary to the prevailing viewpoint (5, 32–36), our results suggest that the antidyskinetic effects of AMT are not a consequence of NMDAR antagonism, but rather of its ability to block Kir2 K^+ channels that control basal dendritic excitability of striatal SPNs. Indeed, at clinically relevant concentrations (≤100 μM), AMT effectively increased both somatic and dendritic excitability of iSPNs and dSPNs. Not only did this augmentation increase the summation of EPSPs, it promoted the induction of NMDAR-dependent LTP in iSPNs from both naive and dyskinetic mice. In contrast, AMT had no effect on LTP induced in dSPNs. Taken together, these results suggest that the antidyskinetic effects of AMT accrue from its ability to lessen the disparity in the activity of dSPNs and iSPNs in the on state following levodopa treatment, when striatal DA concentrations are high and dyskinetic behavior is maximal.

AMT preferentially blocked Kir2 K^+ channels and increased SPN excitability. In agreement with previous studies (13, 14, 24), our experiments demonstrated that AMT inhibited synaptic NMDARs expressed by SPNs. However, in contrast to previous work using bath application of agonist and engagement of extrasynaptic NMDARs, our studies assayed synaptic transmission in ex vivo brain slices. In this biologically relevant scenario, the half-maximal inhibition of NMDAR currents was only achieved at AMT concentrations of approximately 650 μM — well above therapeutically relevant AMT concentrations in the plasma (<50 μM) and brain (48–386 μM) (20, 21).

Within the therapeutically relevant range of plasm concentrations (<50 μM), AMT effectively blocked more than half of the Kir2 K^+ channels expressed in a heterologous expression system and in SPNs recorded in mouse ex vivo brain slices. Kir2 K^+ channels are the principal determinants of the resting membrane potential in SPNs, as they are constitutively open at negative membrane potentials (25, 37). Because they are constitutively open at rest, Kir2 K^+ channels also govern somatodendritic input resistance and the response to synaptic current injection. In both iSPNs and dSPNs, AMT increased neuronal input resistance and excitability as measured by the relationship between the amplitude of intracellular current injection and spike rate. Moreover, as predicted from biophysical principles, increasing SPN input resistance also increased the membrane time constant, slowing the decay of the membrane potential following a perturbation.

To explore the functional implications of AMT-induced changes in membrane properties, SPNs were interrogated using a combination of Ca^{2+} imaging, 2-photon laser uncaging (2PLUG), and patch clamp electrophysiology in ex vivo brain slices. These studies revealed 3 key points. First, by increasing membrane resistance, AMT enhanced bAP propagation into the distal dendrites of SPNs, leading to greater cytoplasmic Ca^{2+} transients in response to spikes triggered in the soma. Second, as expected from the elevation in membrane resistance, AMT increased the amplitude of EPSPs evoked by uncaging glutamate on visualized dendritic spines of SPNs. Third, as predicted by the slowing of the membrane time constant, AMT increased the temporal summation of EPSPs evoked by minimal local stimulation of glutamatergic axons. Taken together, these results demonstrate that AMT block of dendritic Kir2 K^+ channels effectively increased integration of excitatory, glutamatergic synaptic input. Moreover, the enhancement of bAP invasion into dendrites produced by AMT sets the stage for an enhancement — not disruption — of activity-dependent synaptic plasticity in SPNs.

AMT promoted LTP induction. To test the hypothesis that AMT block of Kir2 K^+ channels enhances long-term synaptic plasticity in SPNs, STDP protocols were used. In perforated-patch recordings from ex vivo brain slices, these protocols evoke Hebbian forms of synaptic plasticity in both iSPNs and dSPNs (8–12, 38). Repeated pairing of a glutamatergic EPSP with a coincident or trailing (<5 ms) bAP that produces a depolarization of sufficient magnitude to unblock NMDARs promotes LTP; the Ca^{2+} influx through NMDARs is necessary for SPN LTP. In contrast, repeated pairing of a postsynaptic bAP with a trailing (10 ms) glutamatergic EPSP produces LTD, because by the time that synaptically released glutamate binds to NMDARs, the bAP depolarization has decayed back into a range where Mg^{2+} blocks NMDARs (30). By slowing the decay of the dendritic membrane potential after the bAP, AMT should broaden the time window in which the bAP is capable of producing sufficient depolarization to allow NMDAR opening. In addition, AMT should enhance the depolarization produced by opening of synaptic AMPARs, further augmenting NMDAR engagement. Indeed, even with pairing of a bAP with a trailing EPSP that normally induced LTD, AMT promoted a robust LTP in iSPNs. This was true in both naive iSPNs and those from mice modeling LID.

As outlined above, it is widely thought that the antidyskinetic effect of AMT is a result of reducing aberrant LTP in dSPNs during the on state following levodopa treatment (5, 32–36). To verify that AMT does not have any unidentified off-target effects that might disrupt LTP, dSPNs in both naive and LID mice were studied using the same approaches. As expected, STDP LTP was intact in dSPNs in both preparations and AMT had no effect on LTP induction. Taken together, these data falsify the hypothesis that AMT is attenuating LID by antagonizing NMDARs and disrupting the induction of LTP in SPNs during the on state following levodopa administration.

Why is AMT antidyskinetic? At present, the network mechanisms underlying LID are incompletely understood. A central feature of current thinking is that in the later stages of PD the administration of high doses of levodopa results in a sustained elevation in striatal DA concentration. This sustained elevation undoubtedly results in an abnormally prolonged activation of D1Rs expressed by dSPNs. Through their coupling to intracellular signaling cascades, D1Rs not only increase the intrinsic excitability of dSPNs and the induction of LTP at glutamatergic synapses,

they also activate immediate early genes like Fos that alter dSPN gene expression (39). Indeed, recent work using an elegant combination of Fos-TRAP (targeted recombination in active populations) and optogenetic methods has shown that elevated spiking in a subpopulation of dSPNs in the dorsolateral striatum is necessary for levodopa-induced dyskinetic behavior in mice (40). What these studies do not demonstrate, however, is the sufficiency of dSPN activation for the emergence of LID. In contrast to dSPNs, striatal iSPNs express D2Rs that suppress intrinsic excitability and promote LTD at axospinous glutamatergic synapses (28). In the on state, when striatal DA levels are high, iSPNs are strongly inhibited (8, 41). In fact, during this period, iSPN synaptic strength is depressed enough to result in frank spine elimination (Zhai et al., unpublished observations).

How are these changes linked to dyskinetic movement? In vivo recording of striatal activity of behaving mice has led to the insight that rather than simply opposing one another, iSPN and dSPN ensembles work together to control purposeful movement (42). The current thinking is that dSPN ensembles endorse contextually appropriate actions, whereas iSPN ensembles suppress competing, inappropriate actions. Thus, following high doses of levodopa, the imbalance in activity of these 2 motor control circuits — rather than simply hyperactivation of dSPNs — is likely to be responsible for the inability to suppress unwanted dyskinetic movement. Indeed, elegant chemogenetic studies by Alcacer et al. (15) have shown that either suppression of dSPN excitability or elevation in the excitability of iSPNs in the on state resulted in attenuation of LID in mice.

Our data are nicely aligned with this model of LID. In the on state, AMT had no effect on dSPN LTP, as the excitability of these neurons was already maximal due to the sustained stimulation of D1Rs. However, AMT profoundly enhanced iSPN excitability and LTP induction in the on state, even to the extent of disrupting the normal timing dependence of synaptic plasticity. In so doing, AMT should help iSPN ensembles counterbalance aberrant activation of dSPN ensembles that trigger unwanted, dyskinetic movements. Our results also suggest that the antidyskinetic effects of $mGluR_5$ antagonists (43) may stem from their ability to attenuate aberrant LTD in iSPNs in the on state. Lastly, although not explored in our study, AMT may diminish off time as levodopa levels decline by diminishing the imbalance between hyperexcitable iSPNs and hypoexcitable dSPNs in the off state (44).

In summary, our studies suggest that the antidyskinetic effects of AMT stem not from its interaction with NMDARs, but rather from its ability to block Kir2 K^+ channels in striatal SPNs. This block increased SPN excitability and promoted LTP induction, in principal diminishing the disparity in iSPN and dSPN excitability in the presence of sustained elevations in striatal DA. By rebalancing the striatal movement control circuitry, AMT may diminish LID severity.

Methods

Animals. Male C57BL/6 mice expressing tdTomato or EGFP under control of either the *Drd1a* or *Drd2* receptor regulatory elements (NINDS GENSAT BAC Transgenics Project, Rockefeller University, New York, New York, USA) used for this study were hemizygous for these transgenes. All mice were 8–10 weeks of age before stereotaxic surgery.

Cell culture. CHO-K1 cells (American Type Culture Collection) stably transfected with KCNJ2 (Kir2.1) were grown in F-12 nutrient mixture medium supplemented with fetal bovine serum, penicillin, and streptomycin plus G418 (600 μg/mL) at 37°C in 5% CO_2.

Slice preparation and electrophysiology. Mice were deeply anesthetized intraperitoneally with a mixture of ketamine (50 mg/kg) and xylazine (4 mg/kg) and perfused transcardially with 5–10 mL of ice-cold artificial CSF (aCSF) composed of (in mM) 125 NaCl, 2.5 KCl, 1.25 NaH_2PO_4, 2.0 $CaCl_2$, 1.0 $MgCl_2$, 26 $NaHCO_3$ and 10 glucose (305 mOsm/L). Parasagittal slices were cut in ice-cold external solution containing (mM) 110 choline chloride, 26 $NaHCO_3$, 1.25 NaH_2PO_4, 2.5 KCl, 0.5 $CaCl_2$, 7 $MgCl_2$, 11.6 sodium ascorbate, 3.1 sodium pyruvate, and 5 glucose (305 mOsm/L).

Individual slices were transferred to a recording chamber after incubation and were perfused continuously (2–3 mL/min) with carbogenated aCSF. Experiments were performed in the dorsolateral striatum at elevated temperature (30°C–32°C). Patch pipettes were loaded with internal solution containing (mM) 120 CsMeSO_3, 15 CsCl, 8 NaCl, 10 HEPES, 0.2 EGTA, 10 TEA chloride, 5 QX-314, 2 Mg-ATP, and 0.3 Na-GTP (305 mOsm/L) for whole-cell voltage-clamp recordings; or 115 K-gluconate, 20 KCl, 1.5 $MgCl_2$, 5 HEPES, 0.2 EGTA, 2 Mg-ATP, 0.5 Na-GTP, and 10 Na-phosphocreatine (280 mOsm/L) for whole-cell current-clamp recordings. All the recordings were made using MultiClamp 700B (Molecular Devices) amplifiers, and signals were filtered at 2 kHz and digitized at 10 kHz. Data were discarded when the series resistance (voltage-clamp) or input resistance (current-clamp) changed more than 20% over the time course of the experiment. For perforated-patch recordings, the internal recording solution was composed of (in mM) 125 K$MeSO_4$, 14 KCl, 2 $MgCl_2$, 0.2 EGTA, and 10 HEPES. Amphotericin B was used to achieve electrical access through the perforated-patch method.

Long-lasting synaptic plasticity was induced using protocols consisting of subthreshold synaptic stimulation paired with somatically induced action potentials (APs) at theta frequency (5 Hz). These protocols consisted of 10 trains of 10 bursts repeated at 0.1 Hz, with each burst composed of 3 APs preceded by 3 EPSPs at 50 Hz (pre-post timing pairing, +5 ms) or 3 APs followed by 1 EPSP (post-pre timing pairing, –10 ms). To ensure induction of consistent synaptic plasticity, postsynaptic neurons were depolarized to –70 mV from their typical resting membrane potentials (–85 mV) during their induction. $GABA_A$ was blocked by the bath application of gabazine (10 μM).

Automated electrophysiology. Automated patch-clamp recording was performed at room temperature using the Syncropatch 768 PE platform (Nanion Technologies) as previously described (45). Single-hole, 384-well recording chips with medium resistance (2–4 MΩ) were used in this study. External solution contained (in mM) 140 NaCl, 4 KCl, 2.0 $CaCl_2$, 1 $MgCl_2$, 10 HEPES, and 5 glucose (pH 7.4). The composition of the internal solution was (in mM) 60 KF, 50 KCl, 10 NaCl, 20 EGTA, and 10 HEPES (pH 7.2). Whole-cell currents were recorded in the whole-cell configuration at –120 mV, 250 ms after the start of the voltage pulse from a holding potential of –60 mV before and after addition of various concentrations of AMT or vehicle. Whole-cell currents were not leak subtracted. The contribution of background currents was determined by recording whole-cell currents at the end of the experiment after addition of $BaCl_2$ (5 mM). Only $BaCl_2$-sensitive currents were used for analysis.

Mouse unilateral 6-OHDA model and LID. Mice were anesthetized with an isoflurane precision vaporizer, placed in a stereotaxic frame, and a hole was drilled over the medial forebrain bundle. After exposing the skull, 3.5 mg/mL free-base 6-hydroxydopamine (6-OHDA) hydrobromide with 0.02% ascorbic acid was injected using a calibrated glass micropipette at the following coordinates: AP, –0.7; ML, –1.2; and DV, –4.75. Three weeks after surgery, the degree of damage to nigrostriatal DA neurons was assessed with a forelimb-use asymmetry test (8). One day after the cylinder test, mice underwent behavioral testing for abnormal involuntary movements (AIMs) following L-DOPA treatment, as previously described (8). Behavioral testing occurred every other day for a total of 5 or 6 test sessions. Animals received 3 and 6 mg/kg L-DOPA for the first 2 and last 3 or 4 behavioral sessions, respectively. Benserazide was coadministered at 12 mg/kg to inhibit peripheral conversion of L-DOPA to DA. AIMs (axial, limb, and orolingual movements) were rated as previously described (8). Each animal was observed individually for 1 minute every 20 minutes for 2–3 hours. Physiological experiments were performed 1 hour after the last L-DOPA administration.

Ca^{2+} imaging and 2PLUG. SPNs were loaded with 50 μM Alexa Fluor 568 and 100 μM Fluo-4 via patch pipette for 15–20 minutes before imaging. 2PLSM was performed with an 810-nm Ultima Laser (Bruker) pulsed at 90 MHz (~250 fs pulse duration) and an Olympus ×60/0.9 NA objective. Red fluorescence of Alexa Fluor 568 was used to visualize the dendritic morphology of SPNs. Whole-cell maximum-projection images of the soma and dendrites were acquired with 0.389-μm pixels with 4-μs pixel dwell time; approximately 100 images were taken with 1-μm focal steps. High-magnification maximum-projection images of dendrites were acquired with 0.15-μm pixels with 10-μs pixel dwell time; approximately 70 images were taken with 0.3-μm focal steps.

A triplet of bAPs was generated by injecting 3 current pulses (each 2 nA, 2 ms) at 50 Hz (46). To measure Ca^{2+} signals, green and red fluorescence signals were collected from 678-Hz line scans in proximal dendrites (~40 μm) and distal dendrites (~100 μm from soma) with 0.194-μm pixels and 10-μs pixel dwell time. Offsets generated by the photomultiplier tubes (Hamamatsu) were measured in the absence of laser light and subtracted from the measurements. Ca^{2+} signals were averaged from 3 trials and quantified as increases in green fluorescence from baseline normalized to the baseline red fluorescence ($\Delta G/R_o$). Decay time constants were derived by fitting the Ca^{2+} signals with a single exponential.

Glutamate uncaging was achieved using a Verdi/Mira laser (Coherent), as previously described (47). MNI-glutamate (5 mM) was superfused over the recorded area at 0.4 mL/h using a syringe pump (WPI) and multibarreled perfusion manifold. The superfusion solution contained (in mM) 124 NaCl, 3 KCl, 2 $CaCl_2$, 1 NaH_2PO_4, 26 HEPES, and 16.7 glucose (pH 7). MNI-glutamate was photolyzed adjacent to individual spines by 1-ms pulses of 720-nm light typically 5–10 mW in power at the sample plane. For each recorded neuron, 1–2 spines (>80 μm) were uncaged and somatic responses recorded in current-clamp configuration. uEPSP amplitudes were measured from averaged (3–5 repetitions) traces.

Chemicals and reagents. Reagents were obtained as follows: amphotericin B, 6-OHDA, levodopa, benserazide (Sigma-Aldrich); APV, NBQX, SR95531 (gabazine), MNI-glutamate (Tocris); and AMT (Adamas Pharmaceuticals).

Statistics. Data analysis was conducted with Igor Pro 6 (WaveMetrics) and Clampfit 9 (Molecular Devices). EPSP amplitude was calculated from 50 sweeps immediately before the start of induction and 20–30 minutes after the end of induction. In studies describing optical or uncaging responses measured from individual spines, the stated *n* indicates the number of spines. Compiled data are expressed as mean ± SEM. Statistical tests were performed using Excel (Microsoft) and SigmaStat (Systat). Nonparametric Mann-Whitney or Wilcoxon's test was used to assess the experiment results, using a probability threshold of 0.05.

Study approval. The present studies involving animal use were reviewed and approved by the Northwestern Institutional Animal Care and Use Committee (Chicago, Illinois, USA).

Author contributions

WS conceived the study and WS and DJS designed the experiments. WS, WR, SZ, and BY carried out electrophysiological recordings, analyzed the data, and prepared the figures. CGV and ALG performed automated electrophysiological studies and prepared the figures. AM provided amantadine. WS and DJS wrote the manuscript. All authors discussed the results and implications and commented on the manuscript at all stages.

Acknowledgments

Funding was provided by the NIH (NS 34696 to DJS) and a contract from Adamas Pharmaceuticals.

Address correspondence to: D. James Surmeier, Department of Physiology, Feinberg School of Medicine, Northwestern University, 303 East Chicago Avenue, Chicago, Illinois 60611, USA. Phone: 312.503.4904; Email: j-surmeier@northwestern.edu. Or to: Weixing Shen, Department of Physiology, Feinberg School of Medicine, Northwestern University, 303 East Superior Street, Chicago, Illinois 60611, USA. Phone: 312.503.6891; Email: wshen@northwestern.edu.

1. Hornykiewicz O. Dopamine (3-hydroxytyramine) and brain function. *Pharmacol Rev*. 1966;18(2):925–964.
2. Kish SJ, Shannak K, Hornykiewicz O. Uneven pattern of dopamine loss in the striatum of patients with idiopathic Parkinson's disease. Pathophysiologic and clinical implications. *N Engl J Med*. 1988;318(14):876–880.
3. Huot P, Johnston TH, Koprich JB, Fox SH, Brotchie JM. The pharmacology of L-DOPA-induced dyskinesia in Parkinson's disease. *Pharmacol Rev*. 2013;65(1):171–222.
4. Fahn S. The history of dopamine and levodopa in the treatment of Parkinson's disease. *Mov Disord*. 2008;23 suppl 3:S497–S508.
5. Blanchet PJ, Konitsiotis S, Chase TN. Amantadine reduces levodopa-induced dyskinesias in parkinsonian monkeys. *Mov Disord*. 1998;13(5):798–802.
6. Jenner P. Molecular mechanisms of L-DOPA-induced dyskinesia. *Nat Rev Neurosci*. 2008;9(9):665–677.
7. Picconi B, et al. Loss of bidirectional striatal synaptic plasticity in L-DOPA-induced dyskinesia. *Nat Neurosci*. 2003;6(5):501–506.
8. Shen W, et al. M4 muscarinic receptor signaling ameliorates striatal plasticity deficits in models of L-DOPA-induced dyskinesia. *Neuron*. 2015;88(4):762–773.
9. Thiele SL, et al. Selective loss of bi-directional synaptic plasticity in the direct and indirect striatal output pathways accompanies generation of parkinsonism and l-DOPA induced dyskinesia in mouse models. *Neurobiol Dis*. 2014;71:334–344.

10. Pawlak V, Kerr JN. Dopamine receptor activation is required for corticostriatal spike-timing-dependent plasticity. *J Neurosci*. 2008;28(10):2435–2446.
11. Shen W, Flajolet M, Greengard P, Surmeier DJ. Dichotomous dopaminergic control of striatal synaptic plasticity. *Science*. 2008;321(5890):848–851.
12. Yagishita S, Hayashi-Takagi A, Ellis-Davies GC, Urakubo H, Ishii S, Kasai H. A critical time window for dopamine actions on the structural plasticity of dendritic spines. *Science*. 2014;345(6204):1616–1620.
13. Blanpied TA, Boeckman FA, Aizenman E, Johnson JW. Trapping channel block of NMDA-activated responses by amantadine and memantine. *J Neurophysiol*. 1997;77(1):309–323.
14. Blanpied TA, Clarke RJ, Johnson JW. Amantadine inhibits NMDA receptors by accelerating channel closure during channel block. *J Neurosci*. 2005;25(13):3312–3322.
15. Alcacer C, Andreoli L, Sebastianutto I, Jakobsson J, Fieblinger T, Cenci MA. Chemogenetic stimulation of striatal projection neurons modulates responses to Parkinson's disease therapy. *J Clin Invest*. 2017;127(2):720–734.
16. Ding Y, Won L, Britt JP, Lim SA, McGehee DS, Kang UJ. Enhanced striatal cholinergic neuronal activity mediates L-DOPA-induced dyskinesia in parkinsonian mice. *Proc Natl Acad Sci U S A*. 2011;108(2):840–845.
17. Chatelain FC, et al. Selection of inhibitor-resistant viral potassium channels identifies a selectivity filter site that affects barium and amantadine block. *PLoS One*. 2009;4(10):e7496.
18. Hiraoka M, Hirano Y, Kawano S, Fan Z, Sawanobori T. Amantadine-induced afterpotentials and automaticity in guinea pig ventricular myocytes. *Circ Res*. 1989;65(4):880–893.
19. Kornhuber J, Weller M, Schoppmeyer K, Riederer P. Amantadine and memantine are NMDA receptor antagonists with neuroprotective properties. *J Neural Transm Suppl*. 1994;43:91–104.
20. Brigham EF, et al. Pharmacokinetic/pharmacodynamic correlation analysis of amantadine for levodopa-induced dyskinesia. *J Pharmacol Exp Ther*. 2018;367(2):373–381.
21. Kornhuber J, et al. Therapeutic brain concentration of the NMDA receptor antagonist amantadine. *Neuropharmacology*. 1995;34(7):713–721.
22. Gong S, et al. A gene expression atlas of the central nervous system based on bacterial artificial chromosomes. *Nature*. 2003;425(6961):917–925.
23. Shuen JA, Chen M, Gloss B, Calakos N. Drd1a-tdTomato BAC transgenic mice for simultaneous visualization of medium spiny neurons in the direct and indirect pathways of the basal ganglia. *J Neurosci*. 2008;28(11):2681–2685.
24. Johnson JW, Kotermanski SE. Mechanism of action of memantine. *Curr Opin Pharmacol*. 2006;6(1):61–67.
25. Shen W, et al. Cholinergic modulation of Kir2 channels selectively elevates dendritic excitability in striatopallidal neurons. *Nat Neurosci*. 2007;10(11):1458–1466.
26. Guo D, Ramu Y, Klem AM, Lu Z. Mechanism of rectification in inward-rectifier K^+ channels. *J Gen Physiol*. 2003;121(4):261–275.
27. Talley EM, Solorzano G, Lei Q, Kim D, Bayliss DA. Cns distribution of members of the two-pore-domain (KCNK) potassium channel family. *J Neurosci*. 2001;21(19):7491–7505.
28. Gertler TS, Chan CS, Surmeier DJ. Dichotomous anatomical properties of adult striatal medium spiny neurons. *J Neurosci*. 2008;28(43):10814–10824.
29. Kreitzer AC, Malenka RC. Endocannabinoid-mediated rescue of striatal LTD and motor deficits in Parkinson's disease models. *Nature*. 2007;445(7128):643–647.
30. Kampa BM, Clements J, Jonas P, Stuart GJ. Kinetics of Mg^{2+} unblock of NMDA receptors: implications for spike-timing dependent synaptic plasticity. *J Physiol (Lond)*. 2004;556(Pt 2):337–345.
31. Traynelis SF, et al. Glutamate receptor ion channels: structure, regulation, and function. *Pharmacol Rev*. 2010;62(3):405–496.
32. Blanchet PJ, Metman LV, Chase TN. Renaissance of amantadine in the treatment of Parkinson's disease. *Adv Neurol*. 2003;91:251–257.
33. Hauser RA, et al. ADS-5102 (amantadine) extended-release capsules for levodopa-induced dyskinesia in Parkinson's disease (EASE LID 2 Study): Interim results of an open-label safety study. *J Parkinsons Dis*. 2017;7(3):511–522.
34. Ko WK, et al. Combined fenobam and amantadine treatment promotes robust antidyskinetic effects in the 1-methyl-4-phenyl-1,2,3,6-tetrahydropyridine (MPTP)-lesioned primate model of Parkinson's disease. *Mov Disord*. 2014;29(6):772–779.
35. Metman LV, Del Dotto P, LePoole K, Konitsiotis S, Fang J, Chase TN. Amantadine for levodopa-induced dyskinesias: a 1-year follow-up study. *Arch Neurol*. 1999;56(11):1383–1386.
36. Verhagen Metman L, Del Dotto P, van den Munckhof P, Fang J, Mouradian MM, Chase TN. Amantadine as treatment for dyskinesias and motor fluctuations in Parkinson's disease. *Neurology*. 1998;50(5):1323–1326.
37. Nisenbaum ES, Wilson CJ. Potassium currents responsible for inward and outward rectification in rat neostriatal spiny projection neurons. *J Neurosci*. 1995;15(6):4449–4463.
38. Fino E, Paille V, Cui Y, Morera-Herreras T, Deniau JM, Venance L. Distinct coincidence detectors govern the corticostriatal spike timing-dependent plasticity. *J Physiol (Lond)*. 2010;588(pt 16):3045–3062.
39. Cenci MA, Konradi C. Maladaptive striatal plasticity in L-DOPA-induced dyskinesia. *Prog Brain Res*. 2010;183:209–233.
40. Girasole AE, et al. A subpopulation of striatal neurons mediates levodopa-induced dyskinesia. *Neuron*. 2018;97(4):787–795.e6.
41. Ryan MB, Bair-Marshall C, Nelson AB. Aberrant striatal activity in Parkinsonism and levodopa-induced dyskinesia. *Cell Rep*. 2018;23(12):3438–3446.e5.
42. Cui G, et al. Concurrent activation of striatal direct and indirect pathways during action initiation. *Nature*. 2013;494(7436):238–242.
43. Rylander D, et al. A mGluR5 antagonist under clinical development improves L-DOPA-induced dyskinesia in parkinsonian rats and monkeys. *Neurobiol Dis*. 2010;39(3):352–361.
44. Hauser RA, et al. Prevalence of dyskinesia and OFF by 30-minute intervals through the day and assessment of daily episodes of dyskinesia and OFF: Novel analyses of diary data from Gocovri pivotal trials. *J Parkinsons Dis*. 2019;9(3):591–600.
45. Vanoye CG, et al. High-throughput functional evaluation of KCNQ1 decrypts variants of unknown significance. *Circ Genom Precis Med*. 2018;11(11):e002345.
46. Carrillo-Reid L, et al. Mutant huntingtin enhances activation of dendritic Kv4 K^+ channels in striatal spiny projection neurons. *Elife*. 2019;8:e40818.
47. Plotkin JL, et al. Impaired TrkB receptor signaling underlies corticostriatal dysfunction in Huntington's disease. *Neuron*. 2014;83(1):178–188.